Physica Medica 137 (2025) 105093

Contents lists available at ScienceDirect

Physica Medica

journal homepage: www.elsevier.com/locate/ejmp

Original paper

Spectral computed tomography thermometry for thermal ablation: applicability and needle artifact reduction

Lennart R. Koetzier [a,b,*], Pim Hendriks [a], Jan W.T. Heemskerk [a], Niels R. van der Werf [c], Mark Selles [d], Aart J. van der Molen [a], Maarten L.J. Smits [e], Marlies C. Goorden [b], Mark C. Burgmans [a]

[a] Department of Radiology, Leiden University Medical Center, Albinusdreef 2, 2333 ZG Leiden, the Netherlands
[b] Department of Radiation Science and Technology, Delft University of Technology, Mekelweg 5, 2628 CD Delft, the Netherlands
[c] Clinical Science Europe, Philips Healthcare, Veenpluis 6, 5684 PC Best, the Netherlands
[d] Department of Radiology, Isala, Dokter van Heesweg 2, 8025 AB Zwolle, the Netherlands
[e] Department of Radiology, University Medical Center Utrecht, Heidelberglaan 100, 3584 CX Utrecht, the Netherlands

ARTICLE INFO

Keywords:
Thermal ablation
Computed tomography
Thermometry
dual-energy CT

ABSTRACT

Background: Effective thermal ablation of liver tumors requires precise monitoring of the ablation zone. Computed tomography (CT) thermometry can non-invasively monitor lethal temperatures but suffers from metal artifacts caused by ablation equipment.

Purpose: This study assesses spectral CT thermometry's applicability during microwave ablation, comparing the reproducibility, precision, and accuracy of attenuation-based versus physical density-based thermometry. Furthermore, it identifies optimal metal artifact reduction (MAR) methods: O-MAR, deep learning-MAR, spectral CT, and combinations thereof.

Methods: Four gel phantoms embedded with temperature sensors underwent a 10- minute, 60 W microwave ablation imaged by dual-layer spectral CT scanner in 23 scans over time. For each scan attenuation-based and physical density-based temperature maps were reconstructed. Attenuation-based and physical density-based thermometry models were tested for reproducibility over three repetitions; a fourth repetition focused on accuracy. MAR techniques were applied to one repetition to evaluate temperature precision in artifact-corrupted slices.

Results: The correlation between CT value and temperature was highly linear with an R-squared value exceeding 96 %. Model parameters for attenuation-based and physical density-based thermometry were −0.38 HU/°C and 0.00039 $°C^{-1}$, with coefficients of variation of 2.3 % and 6.7 %, respectively. Physical density maps improved temperature precision in presence of needle artifacts by 73 % compared to attenuation images. O-MAR improved temperature precision with 49 % compared to no MAR. Attenuation-based thermometry yielded narrower Bland-Altman limits-of-agreement (−7.7 °C to 5.3 °C) than physical density-based thermometry.

Conclusions: Spectral physical density-based CT thermometry at 150 keV, utilized alongside O-MAR, enhances temperature precision in presence of metal artifacts and achieves reproducible temperature measurements with high accuracy.

1. Introduction

Thermal ablation employs thermal energy to minimally invasively treat a wide variety of tumors of limited size including primary and secondary liver and lung tumors, renal cell carcinomas, and bone and soft tissue tumors [1]. The procedure uses an energy generator and a percutaneous electrode to induce coagulative necrosis in tumors through heating (e.g., radiofrequency ablation, microwave ablation, and laser-induced thermal therapy) to a cytotoxic threshold of at least 60 °C, or cooling (e.g., cryoablation) to below −40 °C [2,3].

Interventional radiologists utilize image guidance techniques such as ultrasound, computed tomography (CT), or magnetic resonance imaging

* Corresponding author.
E-mail address: lennartkoetzier@gmail.com (L.R. Koetzier).

https://doi.org/10.1016/j.ejmp.2025.105093
Received 24 April 2025; Received in revised form 25 July 2025; Accepted 19 August 2025
Available online 23 August 2025

(MRI) to precisely position electrodes in the target tumor [4–6]. Besides electrode positioning, imaging assists the physician during and after the procedure to detect any residual tumor or collateral damage to healthy tissue [7,8]. Typically, in CT guidance, a multi-phase pre-ablation scan with a contrast agent visualizes the tumor, and another contrast-enhanced post-ablation scan assesses the treatment's success through changes in tissue perfusion caused by coagulative necrosis [6]. However, tissue perfusion changes may also occur in tumor areas subjected to elevated, but not lethal temperatures, and as a result of vascular occlusion. Difficulties in detecting local residual tumor cells and determining technical success based on tissue perfusion imaging can contribute to high rates of local recurrence [9]. As an alternative to tissue perfusion imaging, tissue temperature can be directly monitored during the ablation procedure. Driven by recent improvements in combined angio-CT systems that have renewed the interest in use of this modality for interventional oncology procedures, CT presents as a non-invasive medium for thermometry that is widely used for planning, probe positioning and treatment confirmation [10].

CT thermometry utilizes the inverse relationship between CT attenuation coefficient and tissue temperature. In this method, thermal expansion (or contraction) causes a change in tissue density, measurable through changes in Hounsfield Unit (HU), thus providing thermal feedback to the physician [11]. Furthermore, in-room CT imaging is especially suitable for thermal ablation due to its speed, high spatial resolution, and the capability to depict tumors using contrast enhancement.

CT thermometry's early experiments in the seventies and eighties demonstrated its potential for non-invasive temperature monitoring, achieving a temperature precision of a fraction of a degree Celsius and a spatial resolution of 1 cm, but issues with reproducibility hindered further development [12,13]. The resurgence of interest in CT thermometry coincided with the introduction of multi-slice CT scanners in 2008, which substantially improved imaging capabilities and reproducibility, but temperature accuracy remained an issue [14,15]. Meanwhile, Frich et al. outlined essential criteria for making non-invasive thermometry clinically viable, such as a spatial resolution below 2 mm, temperature precision below 2 °C, and an acquisition time below 30 s [7].

A recent development in CT thermometry is the use of spectral CT, showing potential to monitor temperature non-invasively with precision reaching below 2 °C in absence of metal artifacts [16–18]. Liu et al. investigated the potential application of using physical density maps, produced with spectral CT, for conducting CT thermometry and found a strong, reproducible correlation between temperature and physical density changes in ex vivo studies [19,20]. While a recent study demonstrated the potential of spectral CT for metal artifact reduction (MAR) for physical density-based thermometry, it did not evaluate the model during active heating with an ablation needle [21]. This leaves open questions regarding the potential impact of gas bubbles or applicator-induced metal artifacts on physical density measurements. In addition, to our knowledge, this is the first study to evaluate deep learning-based metal artifact reduction (DL-MAR) for spectral CT thermometry in microwave ablation, and to directly compare attenuation-based and physical density-based CT thermometry under realistic antenna-induced artifact conditions.

This study investigates the applicability of spectral CT thermometry in monitoring microwave ablation. It compares the reproducibility, precision and accuracy of CT thermometry on attenuation value images from conventional CT, with CT thermometry on physical density maps using spectral CT. Furthermore, it identifies the MAR method — among orthopedic MAR (O-MAR), DL-MAR, spectral CT, or a combination— that provides the highest CT thermometry precision.

2. Materials and methods

2.1. Experimental setup

A homogeneous polyacrylamide gel was produced to mimic the thermal and attenuation properties of a human liver [20]. Thermal heating was performed with a microwave ablation system (EMPRINT, Medtronic, Minneapolis, USA) at a central frequency of 2.45 GHz. The ablation antenna tip was inserted approximately 5 cm deep, parallel to the CT's axial imaging plane (Fig. 1a), to mimic the clinical environment and maximize the presence of metal artifacts. Four metallic k-type thermocouples (PH218, JBC tools, Barcelona, Spain) with 0.2 °C accuracy and diameter of 0.4 mm were used to invasively verify material temperature around the ablation antenna. A temperature logging tool (Labview, National Instruments Corp, Austin, Texas, USA) logged temperature over time with a frequency of 3 Hz. The thermocouples were inserted in separate axial planes at a depth of 4 cm on a horizontal line, positioned approximately 10, 15, 20, and 25 mm from the ablation antenna. The metallic thermocouples generated minimal metal artifacts.

CT imaging was conducted using a dual-layer spectral CT scanner (Spectral CT7500, Philips Healthcare, Best, The Netherlands). For all acquisitions, the tube voltage was set at 120 kV. Multiple exposures were utilized, specifically 150 mAs for high-dose scans ($CTDI_{vol} = 11.6$ mGy), and 75 mAs for low-dose scans ($CTDI_{vol} = 5.8$ mGy). The scans were performed in axial mode with a fixed collimation of 128 x 0.625 mm and a rotation time of 1.0 s. Slice thickness/increment was varied at 1.0/0.5 mm and 2.0/1.0 mm. The field of view was set at 350 mm and the image matrix was set to 512. Reconstructions were performed at the scanner's workstation using iterative reconstruction (iDose 4 – level 3) and a standard smooth kernel (B). Spectral reconstructions included virtual monochromatic images (VMI) at various energy levels (70, 90, 110, 130, and 150 keV), alongside effective atomic number (Z effective) maps. Compared to 120 kVp images, VMIs at energies above 70 keV have been shown to reduce beam-hardening and subsequent metal artifacts from various metallic objects, including biopsy needles [22,23]. Additionally, DL-MAR and an orthopedic metal artifact reduction (O-MAR, Philips Healthcare, Best, The Netherlands) were applied individually or combined (first O-MAR, then DL-MAR). O-MAR iteratively corrects photon starvation and reduces subsequent metal artifacts by removing metal traces in the projection space [24]. This DL-MAR, on the other hand, was trained in image space on CT images with simulated artifacts from orthopedic hardware [25]. Notably, it was not trained on needle-shaped metallic objects in soft tissue, VMI, or the application of O-MAR. The selection of MAR methods was guided by the commercial availability of spectral reconstruction and O-MAR on Philips' spectral CT systems. The DL-MAR algorithm was provided through a research collaboration between Leiden University Medical Center, Isala Zwolle, and Philips Healthcare.

2.2. Methodologies

2.2.1. Attenuation-based thermometry

The temperature dependence of CT attenuation can be derived from the effect of thermal expansion on density. To examine how local temperatures affect the CT number and determine the temperature sensitivity, a regression analysis is conducted on the CT values and the corresponding temperature measurements:

$$\Delta HU = a\,\Delta T + b \tag{1}$$

The parameters temperature sensitivity (a) and intercept (b), measured in [HU/°C] and [HU] respectively, represent how HUs vary with temperature.

2.2.2. Physical density-based thermometry

Recently, a physical density model was developed that relies on VMI

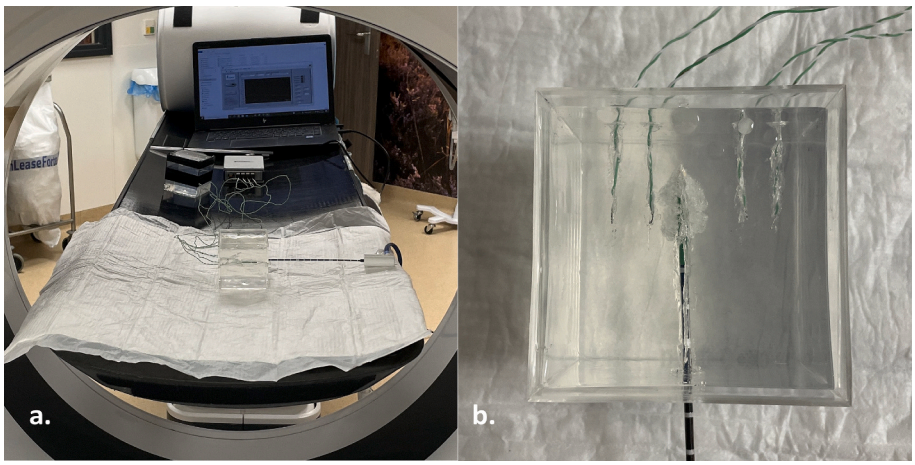

Fig. 1. Photos made of the research setup of the gel phantom. The gel phantom was placed in the gantry of the CT scanner and the ablation antenna was inserted parallel to the axial plane (a). After heating, clear residual gas bubble formation was visible at the tip of the antenna. Temperature sensors were inserted at radial distances of 10, 15, 20 and 25 mm from the ablation antenna as seen in (b).

and effective atomic number and mass maps, denoted by Z_{eff} and A_{eff}, respectively [26]. The effective atomic mass, A_{eff}, is not available on clinical scanners and was obtained by following the methodology of Hwang et al. [26] by fitting a third-order polynomial between the atomic mass and number of the first 30 elements (H, He, Li, etc.), which yielded a good approximation. This model is a parameterized version of the Alvarez & Macovski model for material decomposition [27]. By combining VMI, Z_{eff}, and A_{eff} the following model for physical density was used:

$$\rho = p_1 \frac{A_{eff}\,\mu^{p_2}(E)}{\frac{p_3\, Z_{eff}^{p_4}}{E^{p_5}} + Z_{eff}^{p_6} f_{KN}^{p_7}(E)} \tag{2}$$

where ρ is the physical density (g/cm^3), μ is the linear attenuation coefficient (cm^{-1}) at energy E (keV), and f_{KN} is the dimensionless Klein-Nishina function [27]. For energy levels 70, 90, 110, 130, and 150 keV, parameters p_1, p_2, p_3, p_4, p_5, p_6, and p_7 of this model were fitted to 180 anthropomorphic tissues defined by the International Commission on Radiation Units and Measurements (ICRU) Reports 44 and 46 [28] with corresponding attenuation coefficients from the National Institute of Standard and Technology (NIST) XCOM [26,29]. Physical density maps using VMI at 70——150 keV were generated using Equation (2). Regression analysis on the relative density determines the parameters of the physical density-based model:

$$\frac{\rho(T_0)}{\rho(T)} = \alpha\,\Delta T + \beta \tag{3}$$

where α is the thermal expansion coefficient (°C^{-1}) and β is the dimensionless intercept.

2.2.3. Ablation procedure and scanning protocol

Prior to starting the ablation procedure, a baseline scan was acquired with the ablation antenna and thermocouples in situ (Fig. 1). Subsequently, the gel phantom was heated at an ablation power of 60 W for 10 min and thermocouples recorded the internal temperature. The scanning protocol during the ablation had two phases: in the first 2 min of heating, a series of 7 scans were made at 15-second intervals. During the remaining 8 min an additional 15 scans were performed at 30-second intervals. This procedure was repeated 4 times in 4 separate phantoms, 3 times with a high exposure of 150 mAs, once with a low exposure of 75 mAs. During these four repetitions, a total of 92 scans were made.

2.2.4. Thermometry reproducibility

Both in attenuation and physical density maps, two circular regions of interest (ROI) of 80 mm2 are placed adjacent to the tip of the

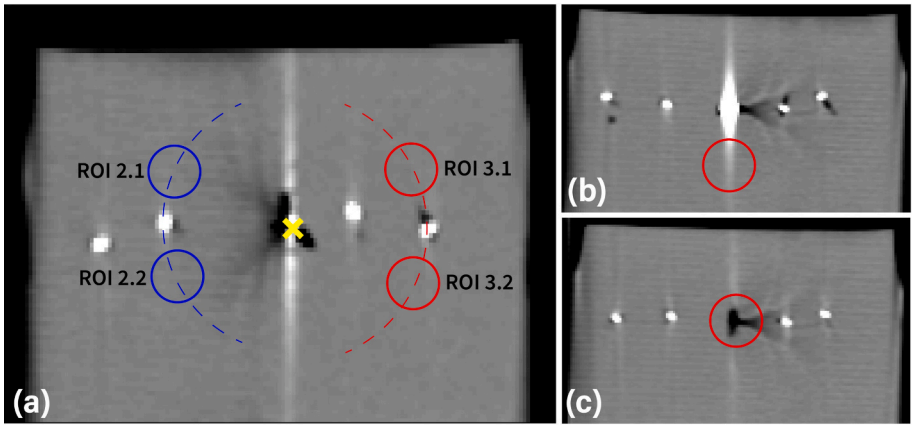

Fig. 2. Sagittal CT images showing regions of interest (ROIs) for monitoring CT values and evaluating temperature precision near metal artifacts: (a) ROIs for temperature sensors 2 (blue) and 3 (red) used to monitor CT values during heating, with the mean and standard deviation calculated assuming radial temperature symmetry around the ablation antenna (yellow cross); ROIs placed lateral to the ablation antenna (b) and in line with the ablation antenna (c) to measure temperature in presence of metal artifacts. The ablation antenna, oriented perpendicular to the image plane, is present in (b) but not in (c).

temperature sensors (Fig. 2). CT value mean and standard deviation are measured. Subsequently, thermometry parameters were fitted using linear regression on ROI measurements and corresponding temperature verification using Equations (1) and (3). The consistency of fit parameters was evaluated using the coefficient of variation (CV), defined as the standard deviation normalized by the mean of the three repetitions. These parameters were used for subsequent temperature precision and accuracy analysis.

2.2.5. Temperature precision

Temperature precision is quantified by propagating the uncertainties in CT images and model parameters to ΔT as measured with CT thermometry. This theoretical metric quantifies the degree of uncertainty in ΔT attributable to uncertainties within the inputs of the thermometry model. By applying the model for attenuation-based thermometry (Equation (1), temperature precision was calculated through error propagation as follows:

$$\delta T = \sqrt{\left(\frac{1}{a}\delta HU(T)\right)^2 + \left(-\frac{1}{a}\delta HU(T_0)\right)^2 + \left(-\frac{1}{a}\delta b\right)^2 + \left(-\frac{\delta a}{a^2}\left(HU(T) - HU(T_0) - b\right)\right)^2} \tag{4}$$

The temperature precision for physical density-based thermometry (Equation (3) was calculated as follows:

$$\delta T = \sqrt{\left(\frac{1}{\alpha\,\rho(T)}\delta\rho(T_0)\right)^2 + \left(-\frac{\rho(T_0)}{\alpha\,\rho(T)^2}\delta\rho(T)\right)^2 + \left(\frac{1}{\alpha}\delta\beta\right)^2 + \left(\left(-\frac{\rho(T_0)}{\rho(T)\,\alpha^2} + \frac{\beta}{\alpha^2}\right)\delta\alpha\right)^2} \tag{5}$$

Here, δHU (T0), δHU(T), δρ(T0), and δρ(T) represent the measurement uncertainty in the pre-ablation images (T0) and intra-ablation images (T). δa, $\delta\alpha$, δb, and $\delta\beta$ represent the standard deviation of the thermometry parameters across three repetitions.

Because a high standard deviation in CT images can be attributed to both high noise levels or severe metal artifacts, the placement of the ROI is varied.By employing two different sets of ROIs, two sets of temperature precision measurements were obtained to quantify the individual sources of uncertainty. First, to determine the temperature precision at varying distances from the ablation antenna, rectangular ROIs of 2 by 2 mm were placed at 10, 15, 20, and 25 mm from the ablation antenna. These ROIs were positioned in two adjacent slices that contained minimal metal artifacts and placed isocentrically around the ablation antenna to eliminate variations in the CT signal due to thermal gradients. The measurement uncertainty in these ROIs was defined as the standard error of the mean.

Secondly, to evaluate the effect of metal artifacts on temperature precision, two additional circular ROIs with a radius of 6 mm were placed—one in line with the ablation antenna and another lateral of the ablation antenna, within the slices most affected by metal artifacts. The measurement uncertainty in these artifact-corrupted ROIs was defined as the standard deviation in the ROI. The temperature precision was calculated across varying combinations of MAR techniques and two slice thicknesses. To assess the effect of increasing slice thickness on precision, normality was first tested using the Shapiro-Wilk test, followed by a paired *t*-test. Additionally, the efficacy of different MAR techniques was compared to no MAR using the Wilcoxon signed-rank test. After Bonferroni correction, results with p-values less than 0.0036 were considered statistically significant. Hedges' g was used to measure the effect size of MAR for temperature precision in the presence of metal artifacts, with the baseline approach being attenuation-based thermometry without MAR.

2.2.6. Accuracy

The CT thermometry models were developed based on the three repetitions with 150 mAs exposure. The model's accuracy was subsequently evaluated using the single 75 mAs repetition that was not

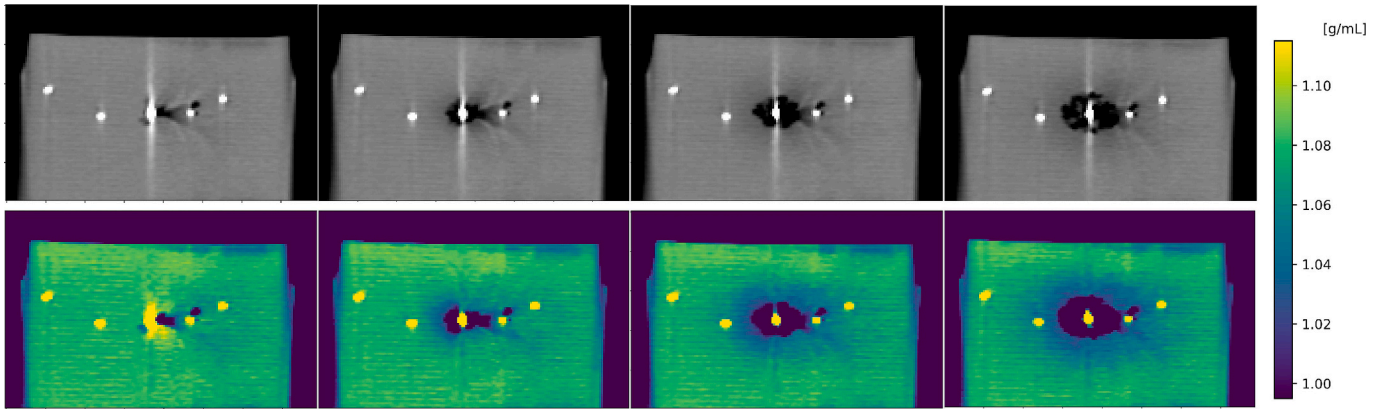

Fig. 3. Example of sagittal CT and physical density images of the liver-mimicking gel phantom before ablation and after 120, 300 and 600 s of ablation (from left to right). Corresponding temperatures recorded by the sensor nearest to the ablation antenna were 18 °C, 55 °C, 70 °C, and 98 °C, respectively. The images show a hypodense area around the ablation antenna. Metal artifacts from the ablation antenna obscure both proximal and distal surrounding tissue. Setting for window/level were 400/60 and 0.12/1.055 for the CT images and physical density maps, respectively.

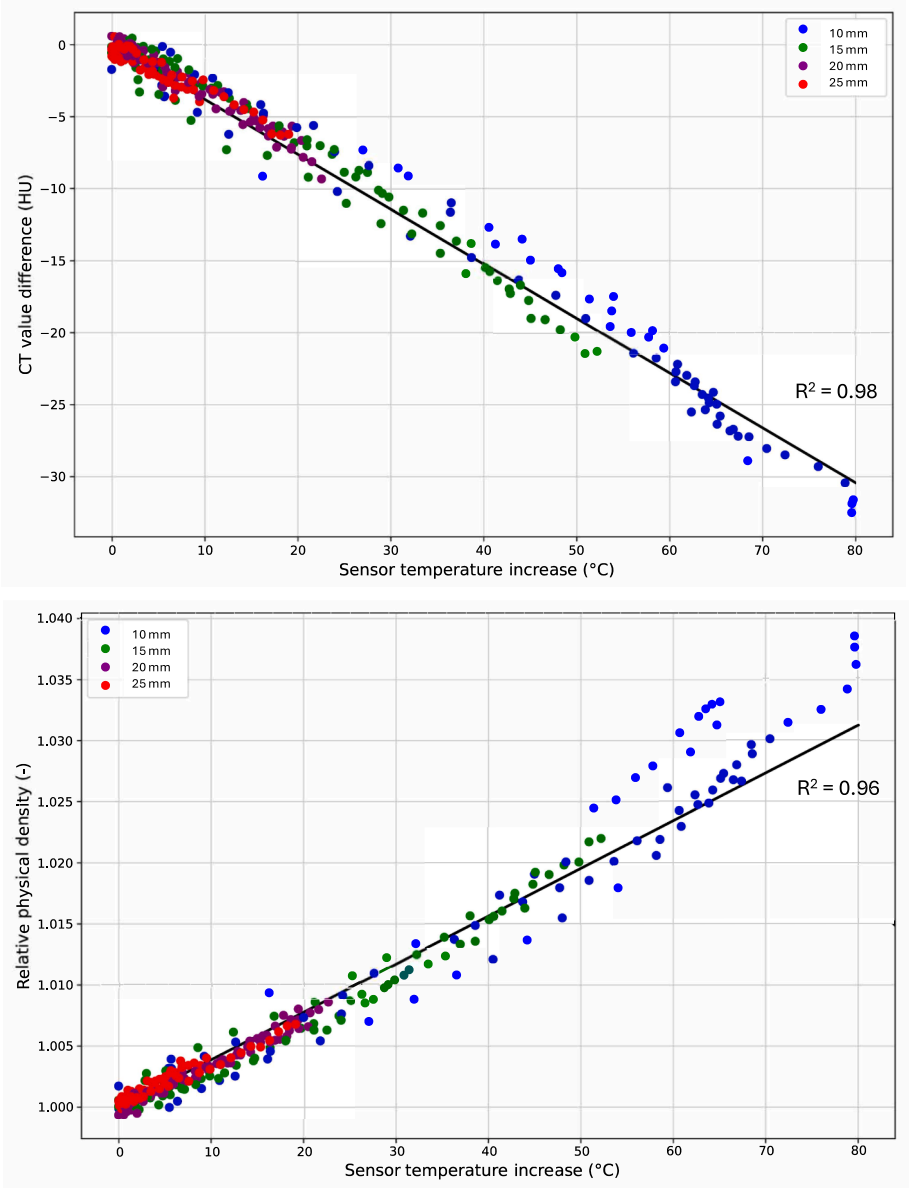

Fig. 4. Regression results of attenuation-based thermometry (top) and physical density-based thermometry at 70 keV (bottom). For the attenuation-based thermometry, linear regression was performed on the combined data of three repetitions to determine the parameters. No metal artifact reduction was applied. The thermal sensitivity (a) was −0.38 HU/°C, while the intercept (b) was 0.52 HU. For the physical density-based thermometry, analysis was also performed on all three repetitions and no additional metal artifact reduction was applied. The thermal expansion coefficient (α) was 0.00039 °C − 1, while the intercept (β) was 0.99. Note that the high R2 indicates a high linearity of the thermal expansion coefficient in this temperature range.

incorporated into the model development. For this, temperature maps were generated and modeled temperatures in proximity to the temperature sensors were recorded by employing ROI measurements. To assess the accuracy of modeled temperatures, a Bland-Altman analysis was performed. This analysis provided the mean-of-difference between the temperature as measured by the thermocouples and modeled temperatures, including the 96 % limits-of-agreement, calculated as 1.969 × standard deviation of differences.

3. Results

3.1. Thermometry reproducibility

Fig. 3 shows the CT and physical density images of the reference scan (before ablation) and after 120, 300, and 600 s of ablation. A strong inverse correlation between HU change and temperature increase was found across the three separate test repetitions (Fig. 4, top). The thermal sensitivity (a) was −0.38 ± 0.0088 HU/°C with intercept (b) of 0.31 ± 0.47 HU. These values led to a CV of 0.023 for a and 1.53 for b, indicating a high reproducibility in attenuation-based CT thermometry for this experiment. The high mean R^2 value over three repetitions of 0.98 ± 0.0054 demonstrated the strong linear relationship between HU change and temperature difference. In a similar vein, physical density images showed a comparable but direct relationship between relative density (ρ(T0)/ρ(T)) and temperature difference (Fig. 4, bottom). The measured thermal expansion coefficient (α) was 0.00039 ± 0.000026 $°C^{-1}$ and the intercept (β) 0.99 ± 0.00054. These results, with a CV of 0.067 for α and 0.0005 for β, similarly reflect the high reproducibility of the CT thermometry in this experiment. The high mean R^2 value over three repetitions of 0.96 ± 0.019 demonstrated the strong linear relationship between relative physical density and temperature difference.

Table 1
Temperature precision heatmap calculated using equations (4) and (5). This metric quantifies the degree of uncertainty in ΔT attributable to uncertainties within the inputs of the thermometry model. Colors demonstrate a superior temperature precision of attenuation-based thermometry and the use of DL-MAR. Additionally, greater slice thickness and distance from the ablation antenna improves precision.

	Slice thickness	**1 mm**				**2 mm**			
	Distance from antenna	10 mm	15 mm	20 mm	25 mm	10 mm	15 mm	20 mm	25 mm
No MAR	Attenuation	6.1	5.2	5.1	5.2	5.2	3.7	3.4	4.1
	PD: 70 keV	7.4	4.9	5.0	4.6	7.4	4.2	3.5	3.7
	PD: 90 keV	7.3	4.8	4.9	4.7	7.3	4.1	3.5	3.7
	PD: 110 keV	7.4	4.8	4.9	4.7	7.4	4.1	3.5	3.8
	PD: 130 keV	7.4	4.9	5.1	4.6	7.4	4.1	3.5	3.7
	PD: 150 keV	7.6	5.0	4.9	4.5	7.5	4.2	3.5	3.7
O-MAR	Attenuation	6.1	5.2	5.1	5.2	5.2	3.7	3.4	4.1
	PD: 70 keV	7.2	4.8	5.0	4.6	7.2	4.1	3.5	3.7
	PD: 90 keV	7.2	4.7	4.9	4.7	7.2	4.0	3.5	3.7
	PD: 110 keV	7.2	4.8	4.9	4.7	7.2	4.0	3.5	3.7
	PD: 130 keV	7.2	4.8	5.1	4.6	7.3	4.0	3.5	3.7
	PD: 150 keV	7.4	4.9	4.9	4.5	7.3	4.1	3.5	3.6
DL-MAR	Attenuation	2.8	1.8	1.5	2.0	2.9	1.9	1.4	1.4
	PD: 70 keV	5.8	3.1	2.3	1.8	5.6	3.3	2.2	1.7
	PD: 90 keV	5.7	3.1	2.2	1.7	5.4	3.2	2.1	1.7
	PD: 110 keV	5.6	3.2	2.2	1.7	5.3	3.2	2.2	1.7
	PD: 130 keV	5.6	3.2	2.2	1.7	5.4	3.2	2.2	1.7
	PD: 150 keV	5.7	3.3	2.3	1.7	5.5	3.3	2.1	1.8
O-MAR + DL-MAR	Attenuation	2.8	1.8	1.5	2.0	2.9	1.9	1.4	1.4
	PD: 70 keV	5.8	3.0	2.3	1.8	5.6	3.3	2.2	1.7
	PD: 90 keV	5.7	3.1	2.2	1.7	5.4	3.2	2.1	1.7
	PD: 110 keV	5.6	3.2	2.2	1.7	5.4	3.2	2.2	1.7
	PD: 130 keV	5.6	3.2	2.2	1.7	5.4	3.2	2.2	1.7
	PD: 150 keV	5.7	3.3	2.3	1.7	5.4	3.3	2.1	1.8

3.2. *Temperature precision in absence of needle artifacts*

An improved theoretical temperature precision was observed with an increase in both distance from the ablation antenna and slice thickness, across all MAR strategies, as shown in the heatmap (Table 1). Attenuation-based thermometry provided better precision close to the ablation antenna compared physical density-based thermometry, but this advantage decreased as the distance from the antenna increased. A nearly constant level of precision was observed as VMI energy increased in physical density-based thermometry ($p > 0.999$). The use of DL-MAR

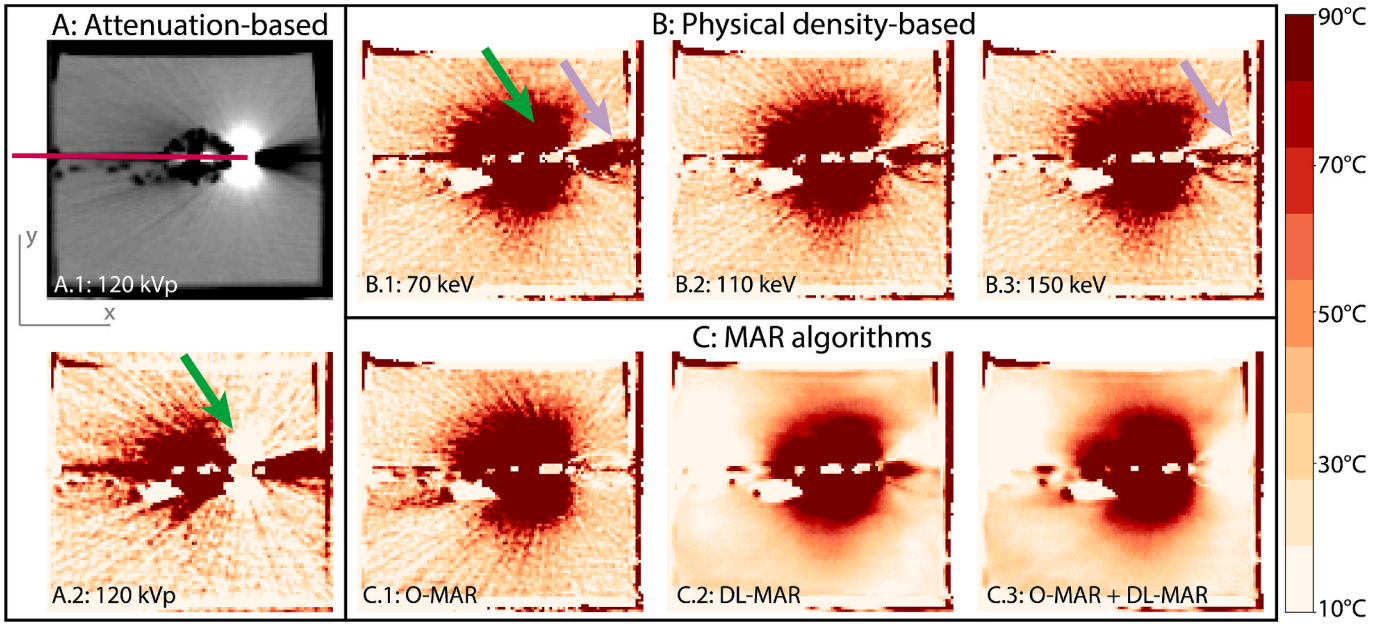

Fig. 5. The effect of various MAR methods on temperature maps A.2, B.1 to B.3, and C.1 to C.3 (window/level = 80/50 °C) after a 10-minute ablation procedure is illustrated. In panel A.1, the ablation antenna's trajectory is depicted as a pink line on an attenuation map (window/level = 400/60 HU). Panel A.2 shows the application of attenuation-based thermometry, which led to substantial artifacts laterally to (green arrow) and in line with the antenna. Panels B.1 through B.3 demonstrate the use of physical density-based thermometry with VMIs at energies of 70, 110, and 150 keV, respectively. This approach resulted in fewer artifacts laterally to the antenna compared to attenuation maps (green arrow in B.1). Increasing VMI energy levels progressively reduced artifacts in line with the antenna (purple arrows in B.1 and B.3). In panel C, O-MAR, DL-MAR, and their combination were applied to 150 keV physical density-based thermometry. O-MAR (C.1) successfully reduced artifacts that were not corrected by spectral CT (B.3). In C.2, DL-MAR reduced image noise but was ineffective at addressing the remaining artifacts missed by spectral CT. In C.3, the combined application of O-MAR and DL-MAR on 150 keV physical density maps demonstrated effective needle artifact reduction by spectral CT and O-MAR, with noise reduction achieved by DL-MAR.

Table 2
Heatmap of temperature precision, calculated using equations (4) and (5) in presence of needle artifacts. Temperature precision quantifies the degree of uncertainty in ΔT attributable to uncertainties within the inputs of the thermometry model. Green colors indicate the enhanced effectiveness of high-energy physical density maps, O-MAR, DL-MAR, and their combination in improving temperature precision. Precision measurements are conducted both inline and laterally to the ablation antenna.

	Slice thickness	**1 mm**		**2 mm**	
	ROI position	In line	Lateral	In line	Lateral
No MAR	Attenuation	523	202	504	190
	PD: 70 keV	549	49	529	44
	PD: 90 keV	316	52	306	47
	PD: 110 keV	219	56	213	50
	PD: 130 keV	173	59	168	53
	PD: 150 keV	149	61	145	56
O-MAR	Attenuation	254	144	245	137
	PD: 70 keV	242	28	234	26
	PD: 90 keV	136	30	131	28
	PD: 110 keV	92	32	90	29
	PD: 130 keV	73	33	71	31
	PD: 150 keV	64	34	62	32
DL-MAR	Attenuation	323	154	312	145
	PD: 70 keV	492	72	476	65
	PD: 90 keV	291	60	279	54
	PD: 110 keV	167	56	158	51
	PD: 130 keV	106	55	99	50
	PD: 150 keV	79	57	74	52
O-MAR + DL-MAR	Attenuation	134	89	127	84
	PD: 70 keV	145	51	139	48
	PD: 90 keV	59	36	58	34
	PD: 110 keV	35	30	34	29
	PD: 130 keV	27	29	26	27
	PD: 150 keV	24	28	23	27

significantly improved temperature precision, showing a substantial decrease in temperature uncertainty compared to when DL-MAR was not used (3.0 vs. 5.5, $p < 0.001$), with a median difference of 2.7 °C. The use of O-MAR slightly improved precision compared to not using MAR (5.4 vs. 5.5, $p = 0.003$). Increasing the slice thickness from 1 to 2 mm significantly improved temperature precision (4.6 vs. 5.5, $p < 0.001$).

3.3. Temperature precision in presence of needle artifacts

A clear improvement of temperature precision was observed with the use of higher energy physical density maps for artifacts in line with the ablation antenna, though this trend was less pronounced for lateral artifacts (Fig. 5, Table 2). Pairwise comparisons revealed that physical density maps at 70 keV did not significantly improve temperature precision compared to attenuation maps. However, at higher energy levels, the improvement of temperature precision became more substantial. Specifically, physical density maps at 90 keV improved temperature precision by an average of 53 % (95 % CI, 11 % − 96 %), with a median difference of 104 °C ($p < 0.001$). At 110 keV, the improvement was 66 % (95 % CI, 47 % − 84 %) on average, with a median difference of 129 °C ($p < 0.001$). At 130 keV, the average improvement reached 71 % (95 % CI, 60 % − 81 %), with a median difference of 127 °C ($p < 0.05$), and at 150 keV, there was a 73 % (95 % CI, 61 % − 84 %) average improvement, with a median difference of 125 °C ($p < 0.001$). O-MAR improved temperature precision on average by 49 % compared to no MAR, with a median difference of 72 °C ($p = 0.001$). DL-MAR showed no significant improvement ($p = 0.01$). The combined use of O-MAR and DL-MAR further improved temperature precision by 60 % on average, with a median difference of 119 °C ($p = 0.001$) (Fig. 5, Table 2). Doubling the slice thickness led to a 6.1 % improvement of temperature precision, with a mean difference of 9 °C ($p < 0.001$). Effect sizes of various MAR approaches for improving temperature precision are given in Table 3.

Table 3
Effect sizes (Hedges' g) of various metal artifact reduction (MAR) methods for enhancing temperature precision in the presence of metal artifacts, using attenuation- based thermometry as the baseline. We propose 150 keV physical density (PD)-based thermometry combined with O-MAR. While the combination of O-MAR and DL-MAR yielded a larger effect size, this increase is likely unrelated to DL-MAR's artifact reduction capabilities.

MAR approach	**g**
PD: 90 keV without MAR	0.5
PD: 110 keV without MAR	0.7
PD: 130 keV without MAR	0.8
PD: 150 keV without MAR	0.9
Attenuation with O-MAR	0.6
PD: 150 keV with O-MAR (proposed)	1.1
Attenuation with DL-MAR	0.4
PD: 150 keV with DL-MAR	1.0
Attenuation with O-MAR and DL-MAR	0.9
PD: 150 keV with O-MAR and DL-MAR	1.2

3.4. Accuracy

The results for attenuation-based thermometry and physical density-based thermometry show high agreement with the temperature verification. Attenuation-based thermometry yielded a mean-of-difference of −1.2 °C, with limits of agreement ranging from −7.7 °C to 5.3 °C (Fig. 6 top). In contrast, physical density-based thermometry demonstrated a mean-of-difference of −0.7 °C, with a range of agreement from −9.5 °C to 8.1 °C (Fig. 6 bottom). When temperatures up to a clinically relevant temperature of 60 °C were analyzed, limits of agreement narrowed to −4.9 °C −4.5 °C and 4.4 °C −6.0 °C for attenuation-based and physical density-based thermometry, respectively, as shown in Supplementary Figs. S1 and S2.

4. Discussion

This study assessed the applicability of spectral CT for non-invasive temperature measurements during microwave ablations in a phantom. Specifically, we compared the reproducibility, theoretical temperature precision in absence and presence of metal artifacts, and temperature accuracy of physical density-based thermometry against attenuation-based thermometry. O-MAR and DL-MAR were also applied to further minimize antenna-induced artifacts. We observed a strong linear correlation between tissue temperature and physical density, with a variation of 6.7 % across three separate ablation procedures. For effective thermal ablation monitoring, clinical targets include a spatial resolution below 2 mm, a CT acquisition time under 30 s, and a temperature precision within 2 °C [7]. In this study, we achieved a temperature precision of 2 °C at a distance of 20 mm from the ablation antenna (Table 1), likely achieved due to the denoising capabilities of DL-MAR on spectral CT. These findings were obtained in a small phantom with a radiation exposure of 150 mAs. Importantly, this 20 mm distance is typically outside the ablation zone.

Physical density maps at 150 keV proved most effective in improving temperature precision in presence of needle artifacts compared to attenuation maps as evidenced by an average significant improvement of 73 % and effect size of 0.9 as shown in Table 2. Furthermore, O-MAR facilitated a 49 % significantly improved temperature precision compared to no MAR as evidenced by an effect size of 0.6 shown in Table 3. However, O-MAR was unable to achieve the clinically desired precision in the presence of metal artifacts under the given conditions. While O-MAR is effective at reducing metal artifacts from large implants in CT scans, it faces challenges with smaller objects like surgical stents or needles, particularly near air, leading to potential uncorrected artifacts [30]. Meanwhile, DL-MAR was trained using simulated data with a variety of orthopedic implants. Consequently, DL-MAR was not specifically trained to reduce metal artifacts from needles or metal in soft tissues such as the liver. The current reduction in metal artifacts suggests that

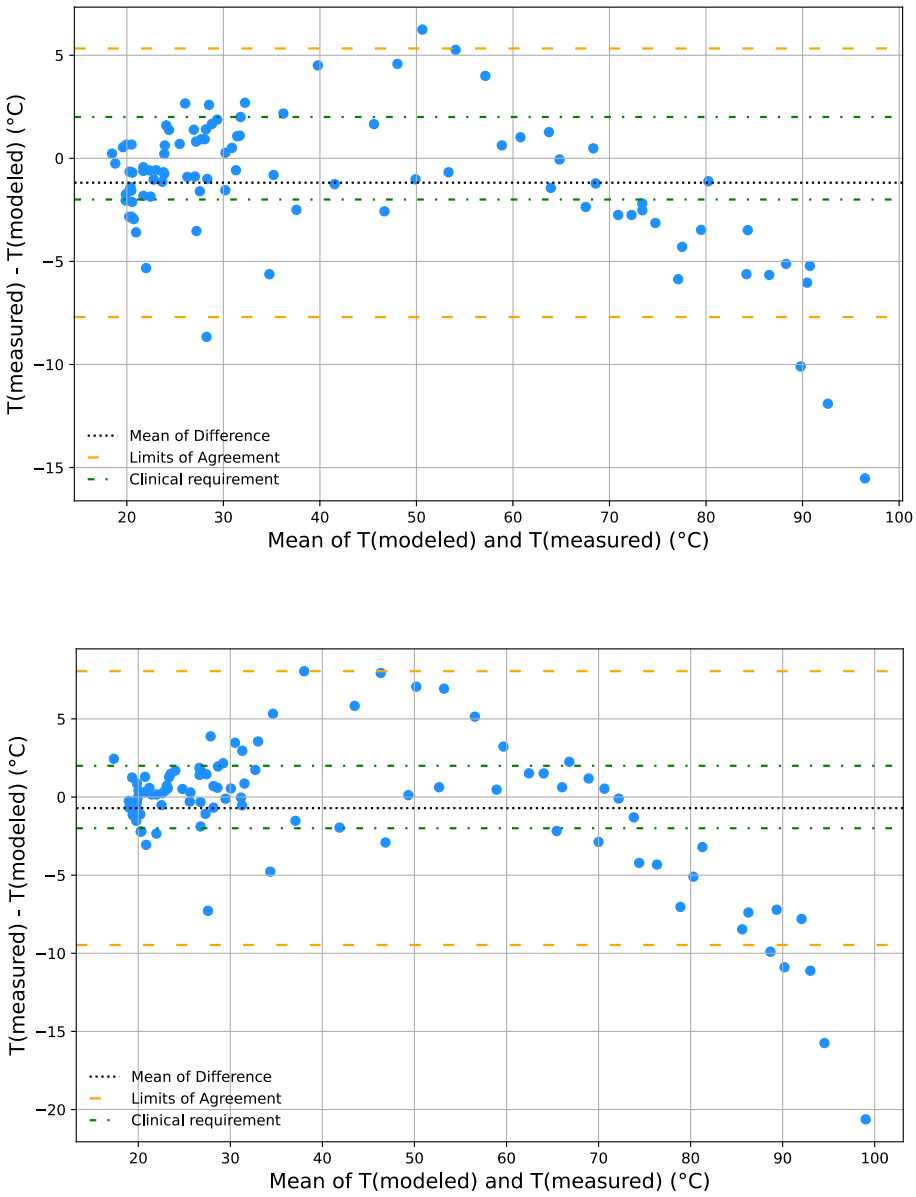

Fig. 6. Comparative Bland-Altman plots for attenuation (top) and physical density-based CT thermometry at 150 keV (bottom). The plots display the difference between measured and modeled temperatures on the y-axis. The x-axis represents the mean temperature of the absolute measured and modeled temperatures. Limits of agreement are marked by the dashed orange lines, while the clinical requirement threshold is indicated by the dashed green line. Note that at temperatures above 35 °C, the accuracy of both models decreases.

further improvements are possible if DL-MAR is also trained on needle-like objects in soft tissue. Until such advancements are made, we propose using 150 keV physical density-based thermometry in combination with O-MAR (g = 1.1). In terms of accuracy, CT thermometry using physical density maps at 150 keV demonstrated high temperature accuracy, with limits of agreement ranging from −9.5 °C to 8.1 °C. Although attenuation-based thermometry achieved higher overall temperature accuracy, likely due to fewer reconstruction steps compared to physical density maps, the benefit of superior temperature precision in presence of needle artifacts outweighs the marginally lower temperature accuracy.

In this study, a thermal sensitivity of −0.38 HU/°C was observed in a phantom using attenuation-based thermometry, consistent with the literature range of −2.00 to −0.23 HU/°C [18,31,32]. A thermal expansion coefficient (α) of 0.00039 $°C^{-1}$ was observed using physical density-based thermometry, which is slightly lower than values reported in prior studies [19,20]. Do et al. investigated iterative MAR, spectral MAR, and a hybrid approach in in vivo pig models. They found that an iterative MAR algorithm (iMAR, Siemens Healthineers) reduced metal artifacts quantitatively for microwave and cryoablation, but not for radiofrequency ablation [33]. In a separate study on biopsy needle artifacts, 80 keV VMI with iterative MAR was identified as the most effective solution [34]. Similarly, Wang et al. demonstrated that a MAR algorithm considering scanner geometry, noise, and anatomy effectively reduced microwave antenna-induced artifacts both quantitatively and qualitatively [35]. Cao et al. were the first to apply deep learning for reducing needle artifacts in kidney cryoablation. Their DL-MAR method effectively reduced artifacts both quantitatively and qualitatively. Ongoing research is expanding this approach to other ablation techniques, needle types, reconstruction parameters, and scanner systems [36].

This study has some limitations. Firstly, a gel phantom, designed to replicate the attenuation and thermal properties of human liver tissue was used [20]. Future research should strive for a more

anthropomorphic approach that better reflects the liver's tissue composition and perfusion. Another limitation of this study is using temperature precision to measure artifact reduction by DL-MAR, which reduces both noise and artifacts. This combined effect complicates isolating artifact reduction. Metrics like peak signal-to-noise ration or structural similarity, which more specifically assess metal artifacts, would have been more appropriate but require ground truth images, which were unavailable. We found that temperature precision improved with distance from the ablation antenna, even though ROIs were designed to reduce the influence of metal artifacts. Some voxels affected by artifacts may have been included, which could explain the improvement at greater distances. Lastly, this study did not assess temperature precision at different radiation doses, an important consideration since CT thermometry likely increases patient radiation exposure due to the need for intra-ablation scans.

Although CT thermometry is based on a simple concept, it has a particular challenge: different tissues, perfusion conditions, and patients can result in different parameters for a thermometry model (α and β). These parameters are impossible to measure in vivo prior to an ablation procedure as it requires a similar approach as the experiments in this study. Additionally, in vivo conditions may differ from animal or ex vivo measurements due to variations in tissue composition and physiological conditions. Therefore, the thermal expansion coefficient, while typically derived from ex vivo or animal studies, can only be approximated for clinical use, and its accuracy remains a subject for further investigation. Also, the thermal properties of the target region may be altered by the intense heat during thermal ablation, which may introduce further errors [11]. Some studies have also reported that the thermometry parameters are not constant with large temperature variations, implying that α and β are a function of temperature. These studies suggest that quadratic [37,38], cubic [39,40] or exponential [41,42] models fit the experimental data better than the linear model. These studies also suggest that tissue heating and cooling affect the CT numbers differently. Future studies, essential for the clinical translation of CT thermometry, should include evaluations that consider tissue heterogeneity, the presence of other anatomical structures, and the heat-sink effect. Research could be structured around experiments using ex vivo liver tissues or phantoms that are perfused, incorporate various tissue types—healthy, cirrhotic, or tumorous—or are subject to intraprocedural movement.

Spectral CT may enhance CT thermometry by leveraging its ability to discriminate between materials, which enables the generation of mappings for specific tissues such as liver, kidney, lung, bone, and tumors. By discriminating tissues and voxel-wise assigning them varying thermometry parameters specific to their composition, more accurate temperature mappings may be generated [40]. For instance, Wang et al. used improved material decomposition capabilities of photon counting CT to develop a deep learning-based thermometry tool [43]. This tool was developed using the linear attenuation coefficient in four energy bins at different temperatures to build a non-linear thermometry model. Although the tool was tested on non-anthropomorphic materials, results showed a mean absolute error of 3.40 °C. This improved tissue differentiation may help to tailor treatments to individual patients, potentially increasing treatment effectiveness and reducing recurrences.

5. Conclusion

Physical density-based thermometry using spectral CT at 150 keV, combined with O-MAR, significantly improves temperature precision in presence of needle artifacts; however, residual artifacts continue to impact temperature precision. Furthermore, physical density-based thermometry demonstrated high overall temperature precision and accuracy, bringing measurement errors closer toward the clinically desired 2 °C. However, attenuation-based thermometry showed slightly greater precision and accuracy in areas without metal artifacts. Additional training of the DL-MAR network on ablation needle artifacts in soft tissue potentially positions it as a one-stop solution for both artifact reduction and noise suppression. Improved tissue differentiation of spectral CT potentially facilitates material-specific temperature maps, offering a promising route for implementing clinical non-invasive thermometry during CT-guided thermal ablations.

Data availability statement

The datasets generated and/or analyzed during the current study are not publicly available due to restrictions but are available from the corresponding author on reasonable request.

Declaration of AI usage

During the preparation of this work the author(s) OpenAI's ChatGPT to enhance the linguistic clarity and overall readability of the manuscript. After using this tool/service, the author(s) reviewed and edited the content as needed and take(s) full responsibility for the content of the publication.

Declaration of Competing Interest

L.R.K. has no relevant conflicts of interest to disclose; **P.H.** has no relevant conflicts of interest to disclose; **J.W.T.H.** has no relevant conflicts of interest to disclose; **N.R.W.** is full-time employee of Philips Healthcare; **M.S.** has no relevant conflicts of interest to disclose; **A.J.M.** has no relevant conflicts of interest to disclose; **M.L.J.S.** is consultant for Philips Healthcare, Terumo/Quirem Medical, and Medtronic; **M.C.G.** has no relevant conflicts of interest to disclose; **M.C.B.** is consultant for Philips Healthcare.

Appendix A. Supplementary data

Supplementary data to this article can be found online at https://doi.org/10.1016/j.ejmp.2025.105093.

References

[1] Crocetti L, de Baére T, Pereira PL, Tarantino FP. CIRSE Standards of Practice on thermal Ablation of Liver Tumours. CardioVasc Intervent Radiol 2020;43:951–62. https://doi.org/10.1007/s00270-020-02471-z.
[2] Nikfarjam M, Muralidharan V, Christophi C. Mechanisms of Focal Heat Destruction of Liver Tumors. J Surg Res 2005;127:208–23. https://doi.org/10.1016/j.jss.2005.02.009.
[3] Gage AA, Baust J. Mechanisms of Tissue Injury in Cryosurgery. Cryobiology 1998;37:171–86. https://doi.org/10.1006/cryo.1998.2115.
[4] Knavel EM, Brace CL. Tumor Ablation: Common Modalities and General Practices. Tech Vasc Interv Radiol 2013;16:192–200. https://doi.org/10.1053/j.tvir.2013.08.002.
[5] Clasen S, Rempp H, Hoffmann R, Graf H, Pereira PL, Claussen CD. Image-guided radiofrequency ablation of hepatocellular carcinoma (HCC): is MR guidance more effective than CT guidance? Eur J Radiol 2014;83:111–6. https://doi.org/10.1016/j.ejrad.2013.09.018.
[6] Crocetti L, Della Pina C, Cioni D, Lencioni R. Peri-intraprocedural imaging: US, CT, and MRI. Abdom Imaging 2011;36:648–60. https://doi.org/10.1007/s00261-011-9750-9.
[7] Frich L. Non-invasive thermometry for monitoring hepatic radiofrequency ablation. Minim Invasive Ther Allied Technol 2006;15:18–25. https://doi.org/10.1080/13645700500470025.
[8] Goldberg SN, Grassi CJ, Cardella JF, Charboneau JW, Dodd GD, Dupuy DE, et al. Image-guided Tumor Ablation: Standardization of Terminology and Reporting Criteria. J Vasc Interv Radiol 2009;20:S377–90. https://doi.org/10.1016/j.jvir.2009.04.011.
[9] Violi NV, Duran R, Guiu B, Cercueil J-P, Aubé C, Digklia A, et al. Efficacy of microwave ablation versus radiofrequency ablation for the treatment of hepatocellular carcinoma in patients with chronic liver disease: a randomised controlled phase 2 trial. LancetGastroenterol Hepatol 2018;3:317–25. https://doi.org/10.1016/S2468-1253(18)30029-3.
[10] Taiji R, Lin EY, Lin Y-M, Yevich S, Avritscher R, Sheth RA, et al. Combined Angio-CT Systems: a Roadmap Tool for Precision Therapy in Interventional Oncology. Radiol Imaging Cancer 2021;3:e210039. https://doi.org/10.1148/rycan.2021210039.
[11] Fani F, Schena E, Saccomandi P, Silvestri S. CT-based thermometry: an overview. Int J Hyperth Off J Eur Soc Hyperthermic Oncol North Am Hyperth Group 2014;30:219–27. https://doi.org/10.3109/02656736.2014.922221.
[12] Fallone BG, Moran PR, Podgorsak EB. Noninvasive thermometry with a clinical x-ray CT scanner. Med Phys 1982;9:715–21. https://doi.org/10.1118/1.595117.
[13] Bydder GM, Kreel L. The temperature dependence of computed tomography attenuation values. J Comput Assist Tomogr 1979;3:506–10. https://doi.org/10.1097/00004728-197908000-00013.

[14] Mahnken AH, Bruners P. CT thermometry: will it ever become ready for use? Int J Clin Pract Suppl 2011:1–2. https://doi.org/10.1111/j.1742-1241.2011.02651.x.
[15] Bruners P, Levit E, Penzkofer T, Isfort P, Ocklenburg C, Schmidt B, et al. Multi-slice computed tomography: a tool for non-invasive temperature measurement? Int J Hyperth Off J Eur Soc Hyperthermic Oncol North Am Hyperth Group 2010;26:359–65. https://doi.org/10.3109/02656731003605654.
[16] Liu LP, Pua R, Rosario-Berrios DN, Sandvold OF, Brown KM, Gang GJ, et al. Phys. Med. Imaging, vol. 12463. SPIE 2023;2023:135–40. https://doi.org/10.1117/12.2649111.
[17] Heinrich A, Schenkl S, Buckreus D, Güttler FV, Teichgräber U-K-M. CT-based thermometry with virtual monoenergetic images by dual-energy of fat, muscle and bone using FBP, iterative and deep learning-based reconstruction. Eur Radiol 2022;32:424–31. https://doi.org/10.1007/s00330-021-08206-z.
[18] Paul J, Vogl TJ, Chacko A. Dual energy computed tomography thermometry during hepatic microwave ablation in an ex-vivo porcine model. Phys Med 2015;31:683–91. https://doi.org/10.1016/j.ejmp.2015.05.014.
[19] Liu LP, Hwang M, Hung M, Soulen MC, Schaer TP, Shapira N, et al. Non-invasive mass and temperature quantifications with spectral CT. Sci Rep 2023;13:6109. https://doi.org/10.1038/s41598-023-33264-2.
[20] Liu LP, Pua R, Rosario-Berrios DN, Sandvold OF, Perkins AE, Cormode DP, et al. Reproducible spectral CT thermometry with liver-mimicking phantoms for image-guided thermal ablation. Phys MedBiol 2024. https://doi.org/10.1088/1361-6560/ad2124.
[21] Liu LP, Brown KM, Perkins AE, Soulen MC, Noël PB. Quantitative metal artifact reduction algorithm for spectral CT thermometry. Conf Proc Int Conf Image Form X-Ray Comput Tomogr 2024;2024:340–3.
[22] Do TD, Heim J, Skornitzke S, Melzig C, Vollherbst DF, Faerber M, et al. Single-energy versus dual-energy imaging during CT-guided biopsy using dedicated metal artifact reduction algorithm in an in vivo pig model. PLoS One 2021;16:e0249921. https://doi.org/10.1371/journal.pone.0249921.
[23] Selles M, van Osch JAC, Maas M, Boomsma MF, Wellenberg RHH. Advances in metal artifact reduction in CT images: a review of traditional and novel metal artifact reduction techniques. Eur J Radiol 2024;170:111276. https://doi.org/10.1016/j.ejrad.2023.111276.
[24] White paper 2012.
[25] Selles M, Slotman DJ, van Osch JAC, Nijholt IM, RuudHH W, Maas M, et al. Is AI the way forward for reducing metal artifacts in CT? Development of a generic deep learning-based method and initial evaluation in patients with sacroiliac joint implants. Eur J Radiol 2023;163:110844. https://doi.org/10.1016/j.ejrad.2023.110844.
[26] Hwang M, Litt HI, Noël PB, Shapira N. Accurate physical density assessments from clinical spectral results. Med. Imaging 2021 Phys. Med. Imaging, vol. 11595, SPIE; 2021, p. 353–9. doi:10.1117/12.2581748.
[27] Alvarez RE, Macovski A. Energy-selective reconstructions in X-ray computerised tomography. Phys MedBiol 1976;21:733. https://doi.org/10.1088/0031-9155/21/5/002.
[28] White DR, Booz J, Griffith RV, Spokas JJ, Wilson IJ. 4. the Composition of Body Tissues. Rep Int Comm Radiat Units Meas 1989;os-23. https://doi.org/10.1093/jicru_os23.1.20.
[29] XCOM: Photon Cross Sections Database. NIST 2009.
[30] Li H, Noel C, Chen H, Harold Li H, Low D, Moore K, et al. Clinical evaluation of a commercial orthopedic metal artifact reduction tool for CT simulations in radiation therapy. Med Phys 2012;39:7507–17. https://doi.org/10.1118/1.4762814.
[31] Pandeya GD, Klaessens JHGM, Greuter MJW, Schmidt B, Flohr T, van Hillegersberg R, et al. Feasibility of computed tomography based thermometry during interstitial laser heating in bovine liver. Eur Radiol 2011;21:1733–8. https://doi.org/10.1007/s00330-011-2106-6.
[32] Bruners P, Pandeya GD, Levit E, Roesch E, Penzkofer T, Isfort P, et al. CT-based temperature monitoring during hepatic RF ablation: feasibility in an animal model. Int J Hyperth Off J Eur Soc Hyperthermic Oncol North Am Hyperth Group 2012;28:55–61. https://doi.org/10.3109/02656736.2011.619155.
[33] Do TD, Haas A, Vollherbst DF, Pan F, Melzig C, Jesser J, et al. Semi-automatic artifact quantification in thermal ablation probe and algorithms for the evaluation of metal artifact reduction. Int J Hyperth Off J Eur Soc Hyperthermic Oncol North Am Hyperth Group 2023;40:2205071. https://doi.org/10.1080/02656736.2023.2205071.
[34] Do TD, Heim J, Melzig C, Vollherbst DF, Kauczor HU, Skornitzke S, et al. Virtual monochromatic spectral imaging versus linearly blended dual-energy and single-energy imaging during CT-guided biopsy needle positioning: Optimization of keV settings and impact on image quality. PLoS One 2020;15:e0228578. https://doi.org/10.1371/journal.pone.0228578.
[35] Wang G, Wang Z, Jin Z. A Novel Metallic Artifact Reduction Technique when using a Computed Tomography-Guided Percutaneous Metallic Antenna to Ablate Malignant Pulmonary Nodules: a Qualitative and Quantitative Assessment. Med Sci Monit Int Med J Exp Clin Res 2020;26:e923541. https://doi.org/10.12659/MSM.923541.
[36] Cao W, Missert A, Parvinian A, Adamo D, Welch B, Callstrom M, et al. Image-Guid. Proced. Robot. Interv. Model., vol. 12928. SPIE 2024;2024:332–43. https://doi.org/10.1117/12.3006552.
[37] Weiss N, Sosna J, Goldberg SN, Azhari H. Non-invasive temperature monitoring and hyperthermic injury onset detection using X-ray CT during HIFU thermal treatment in ex vivo fatty tissue. Int J Hyperth Off J Eur Soc Hyperthermic Oncol North Am Hyperth Group 2014;30:119–25. https://doi.org/10.3109/02656736.2014.883466.
[38] Schena E, Saccomandi P, Giurazza F, Caponero MA, Mortato L, Di Matteo FM, et al. Experimental assessment of CT-based thermometry during laser ablation of porcine pancreas. Phys MedBiol 2013;58:5705–16. https://doi.org/10.1088/0031-9155/58/16/5705.
[39] Li K-W, Fujiwara D, Haga A, Liu H, Geng L-S. Physical density estimations of single- and dual-energy CT using material-based forward projection algorithm: a simulation study. Br J Radiol 2021;94:20201236. https://doi.org/10.1259/bjr.20201236.
[40] Zhang K, Ferrero A, In M-H, Favazza CP. Thermometry mapping during CT-guided thermal ablations: proof of feasibility and internal validation using spectral CT. Phys MedBiol 2024:69. https://doi.org/10.1088/1361-6560/ad45a3.
[41] Strigari L, Minosse S, D'Alessio D, Farina L, Cavagnaro M, Cassano B, et al. Microwave thermal ablation using CT-scanner for predicting the variation of ablated region over time: advantages and limitations. Phys MedBiol 2019;64:115021. https://doi.org/10.1088/1361-6560/ab1a67.
[42] Weiss N, Goldberg SN, Sosna J, Azhari H. Temperature-density hysteresis in X-ray CT during HIFU thermal ablation: heating and cooling phantom study. Int J Hyperth Off J Eur Soc Hyperthermic Oncol North Am Hyperth Group 2014;30:27–35. https://doi.org/10.3109/02656736.2013.860241.
[43] Wang N, Li M, Haverinen P. Photon-counting computed tomography thermometry via material decomposition and machine learning. Vis Comput Ind Biomed Art 2023;6:2. https://doi.org/10.1186/s42492-022-00129-w.